Variable-cell method for stress-controlled jamming of athermal, frictionless grains

Kyle C. Smith*
Department of Materials Science and Engineering, Massachusetts Institute of Technology, Cambridge, Massachusetts 02139, USA

Ishan Srivastava and Timothy S. Fisher†
Birck Nanotechnology Center and School of Mechanical Engineering, Purdue University, West Lafayette, Indiana 47907, USA

Meheboob Alam‡
Engineering Mechanics Unit, Jawaharlal Nehru Centre for Advanced Scientific Research, Jakkur, Bangalore 560064, India
(Received 14 October 2013; revised manuscript received 21 February 2014; published 4 April 2014)

A method is introduced to simulate jamming of polyhedral grains under controlled stress that incorporates global degrees of freedom through the metric tensor of a periodic cell containing grains. Jamming under hydrostatic (isotropic) stress and athermal conditions leads to a precise definition of the ideal jamming point at zero shear stress. The structures of tetrahedra jammed hydrostatically exhibit less translational order and lower jamming-point density than previously described maximally random jammed hard tetrahedra. Under the same conditions, cubes jam with negligible nematic order. Grains with octahedral symmetry having $s > 0.5$ (where s interpolates from octahedra [$s = 0$] to cubes [$s = 1$]) jam with an abundance of face-face contacts in the absence of nematic order. For sufficiently large face-face contact number, percolating clusters form that span the entire simulation box. The response of hydrostatically jammed tetrahedra and cubes to shear-stress perturbation is also demonstrated with the variable-cell method.

DOI: 10.1103/PhysRevE.89.042203 PACS number(s): 45.70.Cc, 45.50.−j, 61.43.−j

I. BACKGROUND

The distinction among the various degrees of jamming has been made by Torquato and co-workers for hard grains [1], and the mapping of such conditions to soft-particle systems has been suggested [2–4]. In collectively jammed systems no collective motions can occur without overlapping other grains, while strictly jammed systems prohibit nonoverlapping global motions (e.g., shear and cell extension) in addition to the collective condition. In contrast, soft-grain jammed systems have been viewed from a mechanical paradigm in which the influence of global deformations has not been explored widely. Approaches for simulating the athermal (i.e., zero-temperature) jamming of soft spheres were pioneered by O'Hern and co-workers [2] by employing structural optimization and molecular dynamics with fixed-cell shape. Jamming has recently been simulated with similar methods for systems of various grain shapes, including ellipses [5], Platonic solids [6–8], arbitrarily shaped polyhedral grains [9], and irregular polydispersed grains [10]. While soft and hard systems of spheres have exhibited consistency among their jammed densities [2–4], disparities have been observed between simulated soft- and hard-tetrahedra packings [6,8,11] and those of experiments [12,13]. Attempts have also been made to correlate the fraction of face-jointed (a stricter condition than a face-face contact, as in Ref. [7]) tetrahedra to density [14]. The extrapolated minimal density (0.625) [14] is very similar to the jamming threshold density of athermal soft tetrahedra (0.62–0.64) [6,7].

Aside from the hard or soft nature of grains, the constraints imposed on granular systems during jamming (e.g., cell shape, stress, and temperature) are not consistent in the literature. Only recently has the importance of global degrees of freedom in the jamming of two-dimensional disk packings been demonstrated [15], and methods are lacking for extension to three dimensions and arbitrary grain shapes. In particular, Dagois-Bohy *et al.* [15] recently demonstrated that jammed packing of disks, with unrelaxed global strain degrees of freedom, were unstable to shear with a negative shear modulus. In addition, recent experiments suggest that metastable jammed states can form under shear [16]. Shape modulation of the periodic cell was an essential part of the densification protocol in hard-tetrahedra systems [11], while cell shape was fixed in previous investigations of soft tetrahedra [6,7].

Other simulations have probed the inherent structures determined by relaxation of randomly oriented soft grains in an isochoric cube-shaped cell [2,17,18]. Such a process replicates the quenching of grains from a high-temperature state [2]. A fixed periodic-cell shape does not reflect the global degrees of freedom present in granular media because this condition generally leads to nonzero shear stress. In the large-system limit fixed-shape cells have been suggested to have negligible influence on the resultant jammed structures [4]. Also, O'Hern and co-workers have considered the effect of shear strain on jamming [5,19], but shear deformations are restricted to specific planes (e.g., the yz, xz, and xy planes of a cube-shaped periodic cell) within their shear-periodic framework (see Ref. [20]). In contrast, variable cells parametrized in terms of lattice vectors, e.g., in Refs. [21–23], enable arbitrary shape deformations that are inherent to the definition of strict jamming [1]. Based on such an approach, Jiao and Torquato [11] asserted that cell-shape variations account for the increased jamming threshold density (0.763) and face-face contact number (greater than two per grain) relative to our previous results on systems jammed in fixed-shape cells (0.62–0.64 jamming threshold [6,7] and one face-face contact per grain [7]).

*kyle.c.smith@gmail.com
†tsfisher@purdue.edu
‡meheboob@jncasr.ac.in

In contrast to granular systems, methods for the simulation of atomistic systems with stress as the controlled quantity have been developed by including cell volume [24] and shape [21,22] variations into system dynamics. At equilibrium in a stress-controlled framework, enthalpy is minimized and when stress is hydrostatic, the framework yields an isobaric, isenthalpic ensemble [21,22]. Such a stress constraint at zero temperature replicates the NPH-ensemble [21] commonly employed in molecular dynamics simulation. In three dimensions, variable-cell deformations have been accommodated in simulations with a parallelepiped (i.e., triclinic) periodic cell whose shape is parametrized by a metric tensor [22].

In this article a variable-cell method is introduced for simulating the athermal jamming of soft frictionless grains under hydrostatic-isotropic loading. In Sec. II a stress-controlled method is introduced for jamming of granular systems under arbitrary states of stress. In Secs. III A, III B, and III C the variable-cell jamming of tetrahedra, cubes, and grains with general octahedral symmetry is presented, respectively. The ability of our method to simulate jamming under both hydrostatic and shear loadings is demonstrated in Secs. III A 2 and III B.

II. ENTHALPY-BASED VARIABLE-CELL SIMULATION METHOD FOR JAMMING

Jamming, or the emergence of rigidity from a liquid state, may occur under conditions of nonzero shear stress, while the ideal jamming point represents the liquid-solid transition in which temperature and shear stress vanish. The density (i.e., volume fraction) at the jamming point is the jamming threshold density ϕ_J. Because jamming processes in which the periodic-cell shape is fixed cannot control shear stress directly, such processes will generally follow a path that does not approach the jamming point when expanded from a jammed state at finite pressure [Fig. 1(a), gray path]. Along such a path, the system will liquify at a density that differs from the jamming threshold density. The principal stresses in a granular material must be identical with no shear-stress component (i.e., exactly hydrostatic or isotropic) to approach the jamming point [Fig. 1(a), red path].

To simulate jamming under hydrostatic conditions (as well as structural response subject to arbitrary applied stresses) the variable-cell method of Souza and Martins [22] is employed here. An arbitrary periodic-cell shape is defined by three lattice vectors, $\boldsymbol{a}_1$, $\boldsymbol{a}_2$, and $\boldsymbol{a}_3$, whose triple forms a 3×3 cell matrix $\boldsymbol{h} = [\boldsymbol{a}_1, \boldsymbol{a}_2, \boldsymbol{a}_3]$. To perform structural optimization efficiently, cell-shape degrees of freedom are represented by the metric tensor $\boldsymbol{g} = \boldsymbol{h}^T \boldsymbol{h}$ [22]. Because the metric tensor is symmetric, optimization needs only be performed over six of its nine elements. Arbitrary shape variations are admissible through changes in components of the metric tensor δg_{ij}, including shear and extension [Fig. 1(b)]. Use of the metric tensor also prevents the occurrence of artificial rigid-body rotations during the optimization routine [22]. Since nonspherical grains have rotational degrees of freedom, the mapping between metric tensor and cell matrix deformations should be irrotational. Though an infinite set of cells, specified by $\boldsymbol{h}$, can satisfy

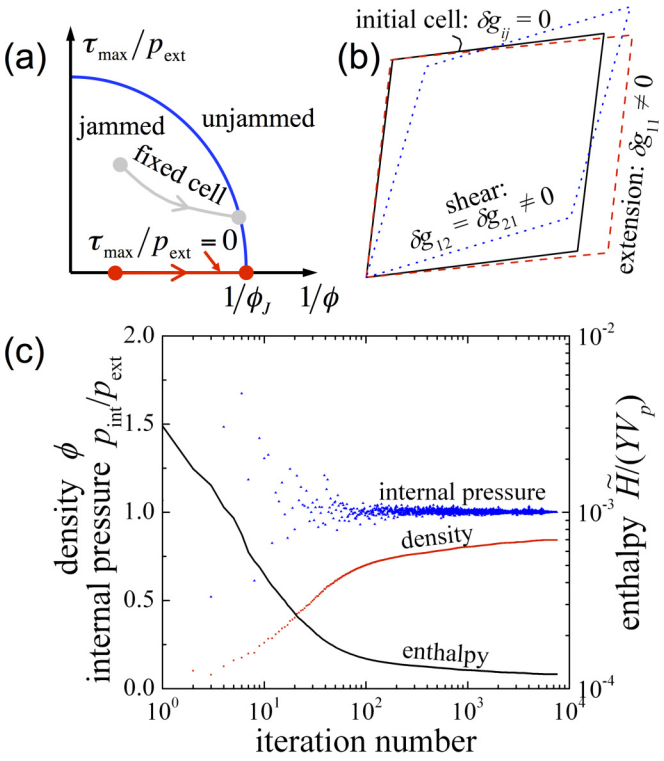

FIG. 1. (Color online) (a) Granular phase diagram [2,25] depicting a hydrostatic unloading process and a fixed-cell-shape expansion process, both of which are at zero temperature. (b) Irrotational global deformations are admitted through variations of the metric tensor describing the symmetric cell matrix $\tilde{\boldsymbol{h}}$. Solid lines represent the edges of the initial cell that can undergo shear and extension to form the cells marked by dotted and dashed lines, respectively. Each of these sample deformations correspond to changes in particular components of the metric tensor δg_{ij}. (c) Variation of density ϕ, internal pressure p_{int}, and generalized enthalpy $\tilde{H}$ with global minimization iterations for a system of 1600 tetrahedra with an external pressure of $p_{\text{ext}} = 10^{-4}Y$.

such irrotational constraints, a unique and simple choice is the symmetric cell matrix $\tilde{\boldsymbol{h}} = \boldsymbol{g}^{1/2}$.[1]

The shape of the variable cell, given by $\boldsymbol{g}$, and the translational and rotational positions of all grains in the assembly $\boldsymbol{r}$ evolve subject to the external state of stress $\boldsymbol{\sigma}_{\text{ext}}$ applied to the cell. The Hamiltonian of this system includes the work done by $\boldsymbol{\sigma}_{\text{ext}}$, in addition to the internal energy $U(\boldsymbol{r})$ arising from elastic intergrain contacts. The quasistatic Hamiltonian at zero temperature (i.e., where kinetic energy is negligible) is the generalized enthalpy $\tilde{H}(\boldsymbol{r}, g_{ij})$ [22]:

$$\tilde{H}(\boldsymbol{r}, g_{ij}) = U(\boldsymbol{r}) + p_{\text{ext}}\sqrt{\det g_{ij}} + g_{ij}\tau^{ij}_{\text{ext}}, \qquad (1)$$

where p_{ext} and $\boldsymbol{\tau}_{\text{ext}}$ are the external pressure and deviatoric-stress tensor that define the external state of stress $\boldsymbol{\sigma}_{\text{ext}} = p_{\text{ext}}\boldsymbol{I}_3 + \boldsymbol{\tau}_{\text{ext}}$ ($\boldsymbol{I}_3$ is the 3×3 identity matrix). Superscript Einstein indices kl of a given tensor $\boldsymbol{\sigma}$ denote a particular contravariant-lattice component σ^{kl} of that tensor.[2]

[1]This can be evaluated with the diagonalized form of $\boldsymbol{g}$.

[2]The contraviant-lattice representation can be determined from a given tensor's Cartesian representation $\boldsymbol{\sigma}_{\text{cart}}$ as $[\sigma^{kl}] = (\det\boldsymbol{h})\boldsymbol{h}^{-1}\boldsymbol{\sigma}_{\text{cart}}(\boldsymbol{h}^{-1})^T$ [22].

Gradients of the enthalpy with respect to metric coordinates g_{ij} must also be expressed to optimize structure [22]:

$$\frac{\partial \tilde{H}}{\partial g_{ij}} = -\tfrac{1}{2}\sigma_{\text{net}}^{ij}. \tag{2}$$

Here the net stress tensor $\boldsymbol{\sigma}_{\text{net}}$ is simply the difference between the internal $\boldsymbol{\sigma}_{\text{int}}$ and external $\boldsymbol{\sigma}_{\text{ext}}$ stresses:

$$\boldsymbol{\sigma}_{\text{net}} = \boldsymbol{\sigma}_{\text{int}} - \boldsymbol{\sigma}_{\text{ext}}. \tag{3}$$

The internal stress tensor $\boldsymbol{\sigma}_{\text{int}}$ is a sum over each contact k:

$$\boldsymbol{\sigma}_{\text{int}} = \frac{1}{\sqrt{\det g_{ij}}} \sum_k \boldsymbol{F}_k \otimes \boldsymbol{l}_k, \tag{4}$$

where $\boldsymbol{F}_k$ and $\boldsymbol{l}_k$ are the force and branch vector of contact k, respectively. In systems of nonspherical grains $\boldsymbol{\sigma}_{\text{int}}$ is only symmetric when contact moments are in equilibrium [26], but its antisymmetric component vanishes as internal degrees of freedom equilibrate during enthalpy minimization.

Equivalent off-diagonal components of the metric tensor evolve identically during optimization (i.e., $\delta g_{ij} = \delta g_{ji}$) and therefore the contribution of both enthalpy gradients [given by Eq. (2)] must be accounted for when optimizing the cell's shape. The translational degrees of freedom of individual grains are optimized in terms of their lattice coordinates, instead of their Cartesian coordinates. The lattice translational coordinates $\boldsymbol{s}_t$ are expressed in terms of their Cartesian coordinates $\boldsymbol{r}_t$ and the cell transformation matrix $\boldsymbol{h}$ as $\boldsymbol{s}_t = \boldsymbol{h}^{-1}\boldsymbol{r}_t$. The enthalpy gradient with respect to the lattice coordinates of a given grain is $-\boldsymbol{h}^T\boldsymbol{F}$, where $\boldsymbol{F}$ is the net force on that grain. Enthalpy gradients with respect to rotational degrees of freedom are equivalent to the internal energy gradients presented in Ref. [6]. Soft, repulsive pair potentials are employed to describe the conservative elastic interactions between grains. For polyhedral grains an overlap potential $E_{\alpha\beta}$ is employed here that depends on the intersecting volume between contacting grains $E_{\alpha\beta} = 0.25 Y V_{\alpha\beta}^2/V_p$ [6], where $V_{\alpha\beta}$ is the intersecting volume between grains α and β, V_p is the volume of an individual grain, and Y is the elastic modulus of the grains.

Finally, the optimization of enthalpy generally proceeds in a computationally inefficient manner when only gradients are employed to inform iterative search directions (e.g., with the conjugate gradient method) because of the drastically contrasting stiffnesses (and even unlike units thereof) among global and internal degrees of freedom. Therefore, the quasi-Newton L-BFGS algorithm [27] was employed to optimize enthalpy with the aid of a specialized data structure [28]. Diagonal preconditioning was also employed to maximize convergence rates of the iterative sequence.

III. RESULTS AND DISCUSSION

The results for variable-cell jamming of tetrahedra, cubes, and grains with octahedral symmetry under conditions of hydrostatic stress, specified by external pressure $p_{\text{ext}} = 10^{-4}Y$, are presented in Sec. III A, III B, and III C, respectively. The isobaric shear response of jammed systems of tetrahedra and cubes are also discussed. Each realization of a given system was initialized with random grain positions and orientations at a dilute density (i.e., volume fraction of grains) of $\phi = 0.001$.[3] During structural optimization, cell shape automatically contracts, and grain positions and orientations evolve subject to the external pressure applied [Fig. 1(c)]. As enthalpy $\tilde{H}$ is minimized the system's density converges toward an equilibrium value [Fig. 1(c)]. Except at very dilute densities the external stress is nearly in equilibrium with the internal force network, as evidenced by the near unity ratio of internal-to-external pressure $p_{\text{int}}/p_{\text{ext}}$ [Fig. 1(c)]. To estimate the jamming threshold density, external pressure was reduced and contact depth was extrapolated, as described in Ref. [6].

A. Jamming of tetrahedra and the difference between variable- and fixed-cell simulation

The packing of tetrahedra has received significant attention experimentally and computationally. Specifically, athermal jammed structures of soft frictionless tetrahedra within a fixed-shape periodic-cell have exhibited strong similarity to the radial distribution functions (RDFs) of experimental packings of tetrahedronlike grains (see [6,8]). Jiao and Torquato [11] reported a density of 0.763 ± 0.005 and 2.21 ± 0.01 face-face contacts per grain in maximally random jammed packings of hard tetrahedra. In contrast, we reported previously a jamming threshold density of 0.634 ± 0.011 (similar to that of monodisperse spheres) and approximately one face-face contact per grain of athermal tetrahedra jammed within a cell of fixed shape [7].

1. *Hydrostatic, variable-cell jamming: Translational order frustration*

To assess the randomness of jammed structures of tetrahedra, the RDF was computed and compared to previous simulated and experimental data [Fig. 2(a)]. The present systems exhibit RDFs very similar to the experimental RDFs of vibrated tetrahedronlike grains [12] and packed tetrahedral dice [13], denoted, respectively, by *VIB* and *dice* in Fig. 2. Despite the initial peak that results from the steric repulsion between tetrahedra, these RDFs exhibit only short-range order (i.e., the RDF is near unity beyond the initial peak). In contrast, the RDFs of so-called maximally random jammed hard tetrahedra [11] (denoted by *MRJ*) and glassy tetrahedra [29] (denoted by *glass*) exhibit several strong peaks absent in all other packings considered, indicating longer-range order in the latter packings [11,29]. The figure also includes the RDF from our prior fixed-cell athermal simulation of 400 tetrahedra [6]. Comparison to the present variable-cell results confirms that the previous fixed-cell simulation predicts higher short-range order, as indicated by the peaks in the range $1 \lesssim r/R_{\text{min}} \lesssim 2$.

[3]Because the present method is stress controlled, the choice of initial density is insignificant. Specifically, if a density is chosen for which any appreciable contact occurs in the initialized state, expansion of the variable cell will occur (instantaneously reducing the density of the granular system) because of the lack of equilibrium between internal and external pressure.

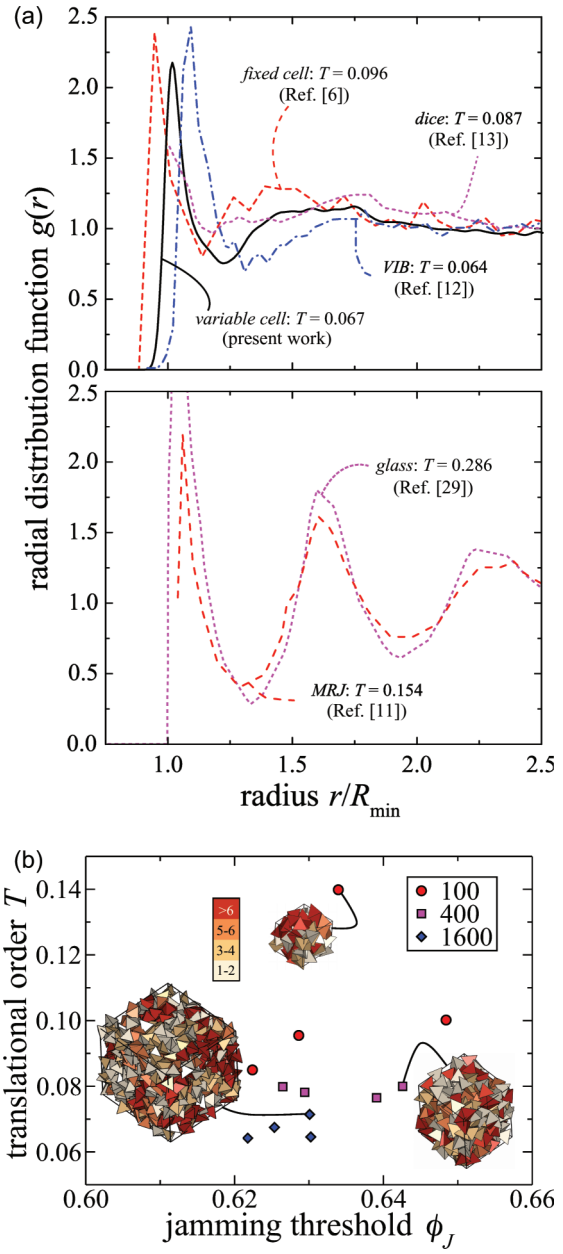

FIG. 2. (Color online) (a) Radial distribution function of hydrostatically jammed tetrahedra at $p_{\text{ext}} = 10^{-4}Y$ and those of other simulated [6,11,29] and experimental studies [12,13] from the literature. Here $2R_{\text{min}}$ is the minimum separation between the centroids of non-overlapping tetrahedra. The translational order parameter T [Eq. (5)] is indicated for each system as well. (b) Translational order T as a function of jamming threshold ϕ_J for multiple realizations of variable cells of various sizes. Selected realizations of grains are colored according to the size of the face-face clusters to which they belong (see legend). Black lines indicate periodic-cell boundaries.

The crystal-independent translational order parameter T was also computed to quantify order in systems of tetrahedra [30]:

$$T = \frac{1}{r_{\text{max}} - r_{\text{min}}} \int_{r_{\text{min}}}^{r_{\text{max}}} |g(r) - 1| dr. \tag{5}$$

The values of T shown in Fig. 2 were obtained by integrating the RDF from a particular r_{min}[4] up to $r_{\text{max}} = 4R_{\text{min}}$ (where $2R_{\text{min}}$ is the minimum distance between the centroids of non-overlapping tetrahedra). Four realizations of each system size (100, 400, and 1600 tetrahedra) were simulated. These results reveal that order generally decreases with system size [see Fig. 2(b)]. On average the translational order parameter for systems of 1600 tetrahedra is 0.064, which is similar to those computed for the experimental structures also considered. By extrapolation, we predict the infinite system to have $T = 0.058$. This order metric confirms that maximally random jammed hard tetrahedra (from Ref. [11]), as well as our prior results from fixed-cell jamming [6], are in fact *less random* than the present soft frictionless tetrahedra jammed athermally in a variable cell under hydrostatic stress.

Tetrahedra jammed in a variable cell exhibit an average jamming threshold density of 0.627 [Fig. 2(b)], which is similar to our previous observations on systems in cells of fixed cubic shape. This finding contrasts with the suggestion of Jiao and Torquato [11] that global degrees of freedom enable tetrahedra to jam with structures having higher jamming threshold density than our previous predictions [6,7]. The discrepancy between athermally jammed tetrahedra and hard tetrahedra [11] is likely related to the inherent thermalizing nature of the Monte Carlo–based method (adaptive shrinking cell [23]) employed to sample the phase-space of hard-grain packings. In a kinetic sense, thermalization enables packed systems to overcome barriers resulting from the low-density jammed structures formed in athermal systems. This notion is also consistent with the granular phase diagram for which higher jamming transition densities are expected for systems at finite temperature than for athermal systems [2,25].

2. *Features that distinguish between structures jammed in variable and fixed cells: Jammed state of stress and shear response*

Using the present stress-controlled approach, we have also generated jammed structures with cubic-cell shape by performing constrained minimization of the generalized enthalpy (i.e., with $\boldsymbol{\sigma}_{\text{ext}} = p_{\text{ext}}\boldsymbol{I}_3$, $\delta g_{11} = \delta g_{22} = \delta g_{33} \neq 0$, and $\delta g_{23} = \delta g_{13} = \delta g_{12} = 0$). This approach for fixed-cell jamming differs from our previous approach (described in Ref. [6]) involving an alternating sequence of isochoric internal-energy minimizations with affine, isotropic strains. We first compare face-face contact numbers $\langle Z_{f-f} \rangle$ between tetrahedra jammed in fixed- and variable-shape cells (Fig. 3(a), assuming that contacts with faces aligned by $< 1^\circ$ are face-face contacts [7]). We observe that fixed-cell shape results in variability of $\langle Z_{f-f} \rangle$ among small-system realizations, but in all cases (including both fixed- and variable-cell structures) $\langle Z_{f-f} \rangle$ is of similar magnitude to our previous predictions [7] but nearly half that reported for maximally random jammed tetrahedra [11]. The grouping of $\langle Z_{f-f} \rangle \approx 1.2$ demonstrates that face-face contact numbers of jammed tetrahedra are insensitive to the cell shape for sufficiently large systems (i.e., $\gtrsim 400$ tetrahedra), contrary to previous claims by Jiao and Torquato [11].

[4]For the fixed-cell simulation from Ref. [6], r_{min} was chosen as the smallest r for which $g(r) = 1$, while for all other cases $r_{\text{min}} = R_{\text{min}}$.

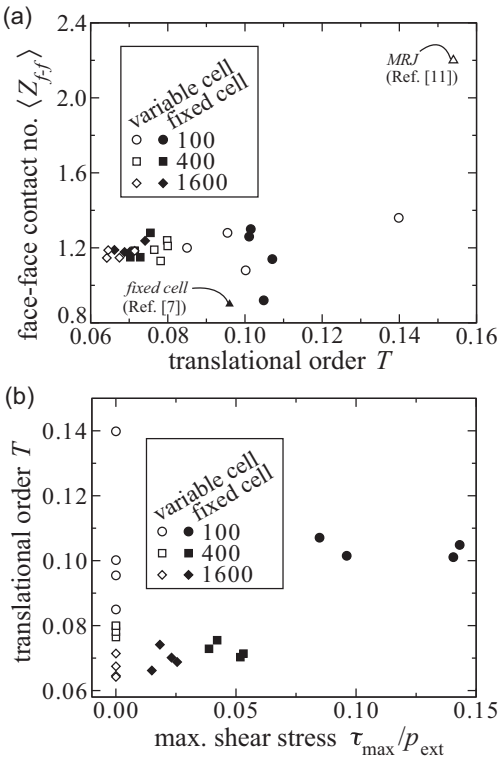

FIG. 3. Structural characteristics of configurations jammed in fixed and variable cells. (a) Face-face contact number as a function of translational order T. Previous results from Refs. [7,11] are shown as reference points. (b) Translational order parameter T as a function of the maximum shear stress for systems jammed in variable and fixed cells.

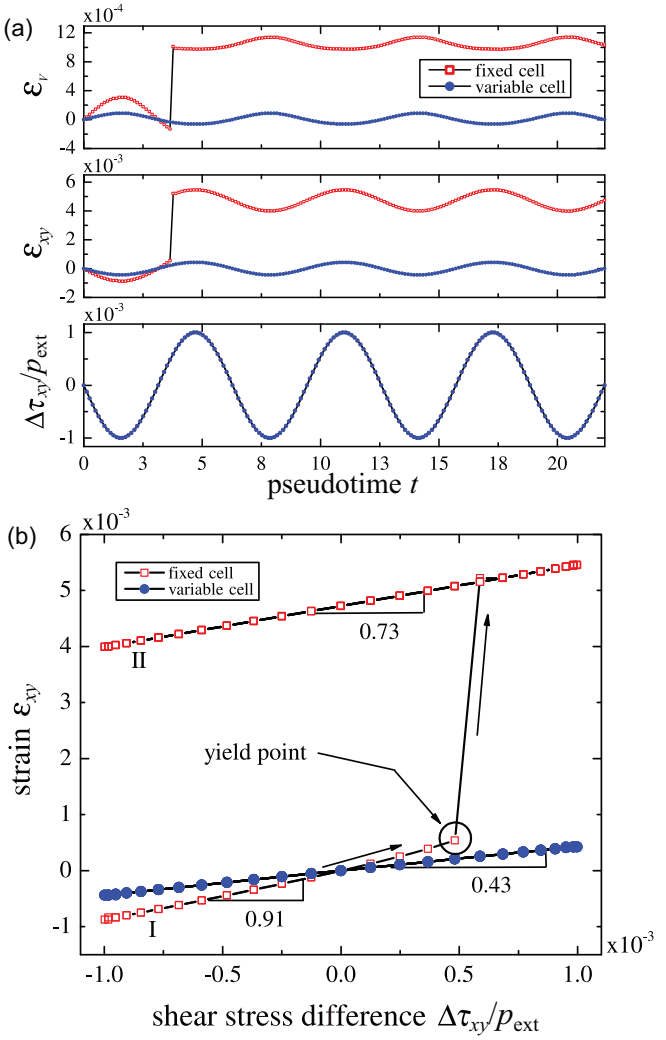

FIG. 4. (Color online) Strain response to oscillatory shear stress of 100 tetrahedra jammed in either a variable or fixed cell at $p_{ext} = 10^{-4}Y$. (a) Time evolution of shear strain ϵ_{xy} and volumetric strain ϵ_V with applied shear-stress difference $\Delta\tau_{xy}$. (b) Lissajous-Bowditch curves of ϵ_{xy} versus $\Delta\tau_{xy}$. For the fixed cell, the yield point is indicated (at which plastic reorganization ensues).

As shown in Fig. 3(b), each realization (whether having a variable- or fixed-shape cell) has a corresponding translational order T and maximum shear stress τ_{max} (i.e., half the difference between the maximum and minimum principal stresses of $\boldsymbol{\sigma}_{int}$). The internal state of stress $\boldsymbol{\sigma}_{int}$ for fixed cells differs from the applied hydrostatic stress $p_{ext}\boldsymbol{I}_3$ because the fixed cell has only one global degree of freedom (the cell volume) instead of the six global degrees of freedom of the variable cell (i.e., g_{11}, g_{22}, g_{33}, g_{23}, g_{13}, and g_{12}). Here τ_{max} depends on the particular configuration being jammed in a fixed cell and consequently exhibits statistical variation among multiple realizations of a given system size. Despite this artificial and unpredictable effect on the mechanical state of the jammed system, the magnitude of τ_{max} decreases (on average) as the size of the fixed cell increases. In other words, the state of stress in fixed cells approaches a hydrostatic state of stress for large systems. As a result, the translational order predicted by fixed cells is very close to that of variable cells for sufficiently large systems because they approach a common state of stress in this limit.

The variable-cell method can also be used to simulate states of stress perturbed from the jammed system (i.e., that due to hydrostatic jamming in either a variable or fixed cell). Using this capability, we applied an oscillatory shear-stress perturbation and simulated the strain response with all global degrees of freedom active (i.e., such that $\boldsymbol{\sigma}_{int} = \boldsymbol{\sigma}_{ext}$ after enthalpy is minimized). We refer to the stress-sequencing variable as pseudotime t in Fig. 4(a) because time is only a surrogate for the order in which stress perturbations occur for the present quasistatic simulations. The xy component of external stress was chosen to vary in psuedotime as $\sigma_{ext,xy}(t) = \sigma^0_{ext,xy} + \Delta\tau_{xy}(t)$, where superscript 0 denotes the jammed value of stress and $\Delta\tau_{xy}(t)$ is the shear-stress difference. The remaining nondegenerate components of external stress were fixed at their jammed values at all instants in pseudotime, i.e., $\sigma_{ext,ij}(t) = \sigma^0_{ext,ij}$. The resulting strains were determined from the evolved metric tensor.[5]

For the small-amplitude oscillations shown in Fig. 4(a), tetrahedra jammed in a variable cell respond elastically with negligible hysteresis. In contrast, tetrahedra jammed in a

[5]The strain tensor was computed as $\boldsymbol{\epsilon} = 0.5[(\boldsymbol{h}_0^T)^{-1}\boldsymbol{g}\boldsymbol{h}_0^{-1} - \boldsymbol{I}_3]$ [21], where $\boldsymbol{h}_0$ is the hydrostatically jammed cell matrix.

fixed cell undergo yielding and plastic reorganization at $\Delta\tau_{xy}/p_{\text{ext}} \approx 5 \times 10^{-4}$ [Fig. 4(a)]. This yield point separates two regimes of elasticity: pre- and postyield (termed I and II, respectively). During the respective elastic regimes both systems undergo antiphase dilation with the applied shear-stress difference, but the plastic-flow event in the fixed cell contracts its volume [Fig. 4(a)]. Also, both the differential shear modulus $G = \partial\Delta\tau_{xy}/\partial\epsilon_{xy}$ and shear strength are enhanced by plastic reorganization for the fixed cell [Fig. 4(b)]. Additionally, the differential shear modulus of the variable cell exceeds that of the fixed cell in both regimes I and II [Fig. 4(b)]. These results demonstrate that configurations jammed in fixed cells are weaker and more compliant than those jammed in variable cells.

B. Jamming of cubes: Nematic order frustration and shear response

Packed cubes exhibit a variety of phases, including ordered space-filling phases [23], but jammed phases also form at a threshold density of ~ 0.8 with strong nematic order in fixed-shape cells of finite size [6]. Smooth grain shapes that resemble cubes (e.g., superellipsoids or superballs, which interpolate between spheres and cubes) have exhibited similar nematic ordering in cells of fixed shape [31,32]. Cubes exhibit three possible nematic ordering directions aligned with cubic faces, denoted by $\hat{u}$. By sorting the three orientation directions of a given cube to different sets based on their alignment with the three nematic directors, a nematic tensor can be computed for each director [33]:

$$\boldsymbol{Q} = N^{-1} \sum_{i=1}^{N} \left(\frac{3}{2} \hat{u}_i \otimes \hat{u}_i - \frac{1}{2} \boldsymbol{I}_3 \right), \tag{6}$$

where i denotes a given grain and the sum loops over all N cubes. From the dominant eigenvalue of a given nematic tensor λ_{max} the uniaxial nematic order parameter is $S_2 = 2\lambda_{\text{max}} - 1$. We report the largest such value among all three nematic directors.

Several realizations of each system size (100, 400, and 1600 cubes) were simulated. One-hundred cube systems tend to form highly ordered structures as a result of the correlated motions between periodic images. As a result, two of the four small systems exhibit artificially high density and the cell shape of these systems strongly deviates from that of a cubic cell [Fig. 5(a), upper right]. For packings of the most cubelike superellipsoids reported in Ref. [31] the average uniaxial nematic order parameter was 0.75; the system of 400 cubes jammed with a fixed cubic cell in our previous work [6] exhibited a dominant uniaxial nematic order parameter of 0.74. Even more ordered crystalline structures have been simulated in thermalized systems [34,35]. In contrast, the realizations of 400 cubes jammed hydrostatically are spread over a large range of order [see Fig. 5(a)] that includes the aforementioned values from the literature. A trend of decreasing order with density is apparent and six of eight 1600-cube realizations exhibit $S_2 \approx 0.2$, which reflects dramatically less nematic order than jammed cubelike grains from the previous reports already described. These cases are indicative of the order expected in the large-system limit.

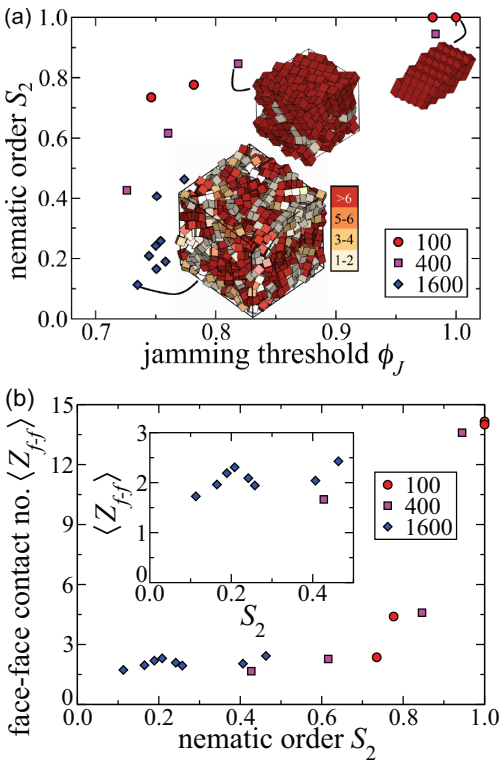

FIG. 5. (Color online) (a) Nematic order parameter S_2 as a function of jamming threshold density ϕ_J for realizations of cubes jammed hydrostatically at $p_{\text{ext}} = 10^{-4}Y$ in a variable cell. Thumbnails of selected configurations are depicted with color according to the number of cubes belonging to the face-face cluster to which a given cube corresponds. Black edges indicate the boundary of the periodic cell. (b) Face-face contact number $\langle Z_{f-f} \rangle$ as a function of nematic order parameter. The inset shows the variation of $\langle Z_{f-f} \rangle$ for small values of S_2.

Despite the lack of long-range nematic order [Fig. 5(a)], large systems of cubes possess an abundance of face-face contacts [approximately two per cube on average assuming that contacts with faces aligned by $< 1^\circ$ are face-face contacts, Fig. 5(b)]. These contacts form clusters that can be similar in size to the simulation cell and a single cluster can contain the majority of grains in small systems [Fig. 5(a)]. For the largest systems simulated though, small clusters having three to four grains are abundant in these structures. These clusters may function as steric defects that frustrate the nematic order of jammed cubes. For sufficiently large $\langle Z_{f-f} \rangle$, clusters can percolate (note that spanning the simulation cell is an insufficient condition for percolation in periodic systems [36]) and these results motivate the exploration of larger systems in which the finite-size scaling of face-face clusters may be quantified.

From a composite-material engineering perspective, the ability to tune cluster percolation with grain shape is useful because transport processes (e.g., heat, mass, and charge transport) are highly sensitive to the extent of clusters (see Refs. [8–10,37]). One way to control cluster percolation is to shear hydrostatically jammed structures and thereby increase order, density, and face-face contact number. To test this hypothesis we have also used the stress-controlled variable-cell

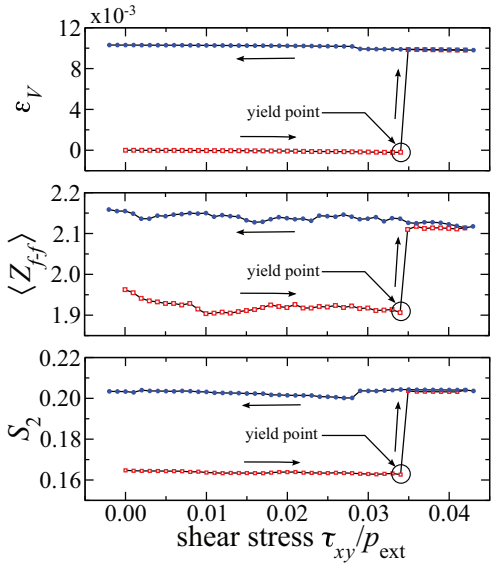

FIG. 6. (Color online) Volumetric strain ϵ_V, face-face contact number $\langle Z_{f-f} \rangle$, and nematic order S_2 as a function of applied shear stress for a system of 1600 cubes, at $p_{\text{ext}} = 10^{-4}Y$.

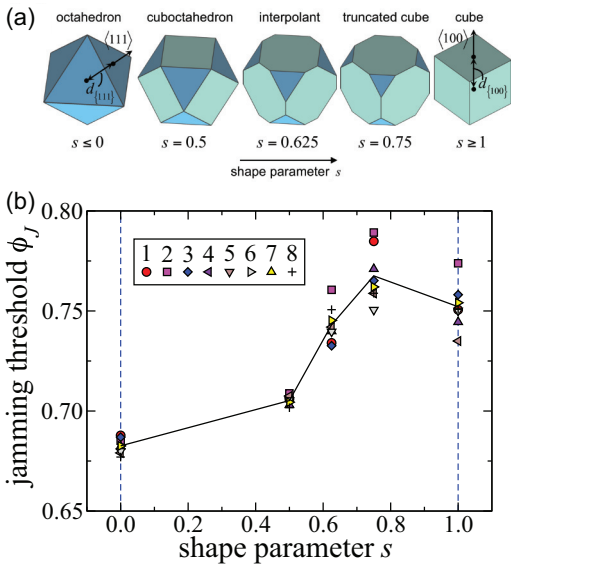

FIG. 7. (Color online) (a) Octahedrally symmetric grain shape as a function of shape parameter s. Green and blue faces lie on {100} and {111} crystallographic planes, respectively, and the directions normal to those planes are indicated. (b) Jamming threshold density ϕ_J as a function of shape parameter s for various realizations of 1600 grains (specified by seed number, indicated in the legend). Black lines were averaged over all realizations of a given grain shape.

method to simulate the response to large shear-stress perturbations of 1600 cubes jammed hydrostatically in a variable cell, as shown in Fig. 6. As shear-stress magnitude increases, mild dilation occurs with near-constant $\langle Z_{f-f} \rangle$ and nematic order until the system yields at $\tau_{xy}/p_{\text{ext}} \approx 0.035$, after which the system contracts, gains more face-face contacts, and becomes more nematic. As shear-stress magnitude is relaxed toward the initial hydrostatic state of stress (i.e., $\tau_{xy} = 0$), the system does not return to the initial level of strain and nematic order before it was sheared. This result suggests that nematic order and face-face contact number in cube systems are sensitive to shear stresses. Thus, shear stress may be used to generate dense, interconnected assemblies of cubes.

C. Jamming of octahedrally symmetry grains: Face-face contact emergence

Because of their dual symmetry, cubes and octahedra belong to a class of grain shapes parametrized by a linear interpolation variable s:

$$s = 0.5(\sqrt{3}d_{\{111\}}/d_{\{100\}} - 1), \tag{7}$$

where $d_{\{111\}}$ and $d_{\{100\}}$ are the distances from the grain's centroid to {111} and {100} crystallographic faces of a given grain shape. As shown in Fig. 7(a), the octahedron ($s = 0$) and cube ($s = 1$) are extremes in this class and several of the Archimedean solids interpolate between them: the truncated octahedron ($s = 0.25$, not shown), cuboctahedron ($s = 0.5$), and truncated cube ($s = 0.75$). Both the Platonic and Archimedean solids have recently received attention with regard to optimal [38] and jammed [6,7,39] packing. Also, the self-assembly of thermalized grains belonging to this class have been explored recently [40,41]. Knowledge of how these grains jam at zero temperature will yield insight into the kinetic barriers that inhibit ordering in thermalized systems. Also, this class of grains is practically useful for bottom-up composite material fabrication because crystallographic structures having octahedral symmetry (e.g., simple cubic or diamond) can form faceted grain shapes with the same symmetries.

Eight realizations of 1600 grains of various shapes having octahedral symmetry are simulated under a hydrostatic pressure of $p_{\text{ext}} = 10^{-4}Y$ in a variable cell. The jamming threshold density ϕ_J exhibits a marked increase as s increases near $s \approx 0.5$ [see Fig. 7(b)]. We also estimated face-face contact numbers $\langle Z_{f-f} \rangle$ (i.e., average number of face-face contacts per grain) based upon the statistics of face-face alignment angles, as in Ref. [7]. While jammed cubes exhibit an abundance of face-face contacts, our previous results suggest that octahedra jam with very few face-face contacts (approximately one per grain on average in a cube-shaped cell [7]). Among the various octahedrally symmetric shapes we have considered, a strong peak in the probability distribution of face-face alignment angle θ_{f-f} (see Ref. [7]) emerges for shapes with $s > 0.5$, as in Fig. 8(a). Assuming that contacts with $\theta_{f-f} < 1^\circ$ are face-face contacts, we estimate the average face-face contact number, as shown in Fig. 8(b). For $0 \leqslant s \leqslant 0.5$ the average face-face contact number $\langle Z_{f-f} \rangle$ is constant at ≈ 0.6, but for shapes with $s > 0.5$, $\langle Z_{f-f} \rangle$ increases linearly and saturates to approximately two contacts per grain. Recall that the jamming threshold density ϕ_J [Fig. 7(b)] follows a similar trend with s, suggesting a correlation between $\langle Z_{f-f} \rangle$ and ϕ_J.

The emergence of many face-face contacts has a dramatic effect on microstructure. In particular, the size of clusters formed by grains connected via face-face contacts has a strong dependence on the number of face-face contacts. The extent of these clusters can have a strong impact on the shear response [7] and the transmission of heat or charge through the granular medium [8,37]. For $s \leqslant 0.5$ the microstructures

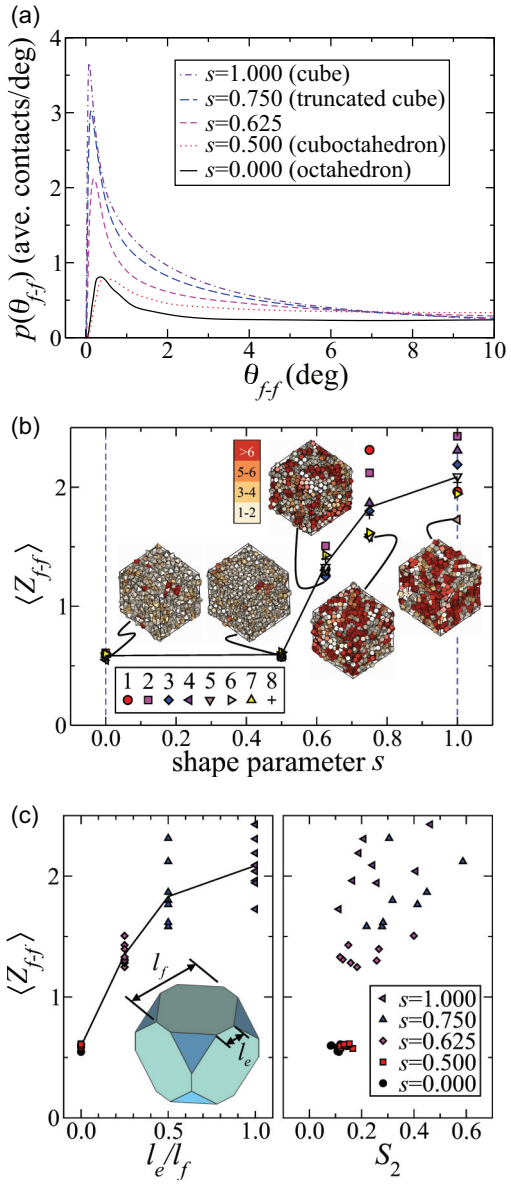

FIG. 8. (Color online) (a) Probability distribution function of face-face alignment angle for jammed systems of 1600 octahedrally symmetric grains at $p_{\text{ext}} = 10^{-4}Y$. These functions were averaged over all realizations and were computed by bounded kernel density estimation [42]. (b) Average face-face contact number $\langle Z_{f-f} \rangle$ for each realization (specified by seed number, indicated in the legend) of a given shape. Grains are colored (see legend) according to the size of the face-face clusters to which they belong for the selected realization (black lines indicate periodic-cell boundaries). (c) Average face-face contact number as a function of edge-to-face length ratio l_e/l_f. Black lines were averaged over all realizations of a given grain shape.

are comprised of minimal-length clusters (dimers having less than two grains) [Fig. 8(b)]. For $s > 0.5$ the microstructures are comprised of a large variety of cluster lengths [Fig. 8(b)], which are long enough in some cases to span the entire simulation cell. This result contrasts strongly with the structures observed for other Platonic solids that did not exhibit face-face cluster percolation in our previous fixed-cell studies [7,8].

Though ordering can induce face-face contact formation, many face-face contacts can form in systems with negligible nematic order (i.e., for $s > 0.5$). A scatter plot of $\langle Z_{f-f} \rangle$ versus S_2 [right panel of Fig. 8(c)] shows that these two parameters are uncorrelated and are not causally related. Even with $S_2 < 0.2$, substantial $\langle Z_{f-f} \rangle$ values are observed. In contrast, a correlated trend of increasing $\langle Z_{f-f} \rangle$ with the length of edges shared by {100} faces on each shape is observed [left panel of Fig. 8(c)]. Only for $s > 0.5$ does such an edge, which is aligned with a ⟨100⟩ direction, appear in the shape's topology. This correlation suggests that the presence of such ⟨100⟩ edges is necessary to form face-face contacts in excess of one per grain (on average).

IV. CONCLUSION

A general variable-cell method for the stress-based jamming of soft, frictionless grains has been introduced via an NPH-type ensemble. The hydrostatic jamming process simulated at zero temperature allows for the probing of the ideal jamming point at zero shear stress specified precisely on the granular phase diagram and yields structures that are highly disordered in the large-system limit. Specifically, jamming under hydrostatic conditions produces structures of tetrahedra with less translational order and cubes with less nematic order than observed previously. The structures formed by hydrostatic jamming of grains with octahedrally symmetric shapes having $s > 0.5$ [Eq. (7)] exhibit larger face-face contact numbers compared to other grain shapes (e.g., tetrahedra [7]). Face-face contacts are promoted by the presence of edges shared among intersecting {100} faces and can form percolating clusters that span the whole simulation box. In addition, the versatility of the present method to simulate jamming under both hydrostatic and shear loadings has been demonstrated.

ACKNOWLEDGMENT

The authors acknowledge the Indo–US Science and Technology Forum for supporting Purdue-JNCASR exchanges through the Joint Networked Centre on Nanomaterials for Energy (Award No. 115-2008/2009-10).

[1] S. Torquato and F. H. Stillinger, J. Phys. Chem. B **105**, 11849 (2001).
[2] C. S. O'Hern, L. E. Silbert, A. J. Liu, and S. R. Nagel, Phys. Rev. E **68**, 011306 (2003).
[3] A. Donev, S. Torquato, F. H. Stillinger, and R. Connelly, Phys. Rev. E **70**, 043301 (2004).
[4] C. S. O'Hern, L. E. Silbert, A. J. Liu, and S. R. Nagel, Phys. Rev. E **70**, 043302 (2004).

[5] M. Mailman, C. F. Schreck, C. S. O'Hern, and B. Chakraborty, Phys. Rev. Lett. **102**, 255501 (2009).
[6] K. C. Smith, M. Alam, and T. S. Fisher, Phys. Rev. E **82**, 051304 (2010).
[7] K. C. Smith, T. S. Fisher, and M. Alam, Phys. Rev. E **84**, 030301 (2011).
[8] K. C. Smith and T. S. Fisher, J. Heat Transfer **135**, 081301 (2013).
[9] K. C. Smith, P. P. Mukherjee, and T. S. Fisher, Phys. Chem. Chem. Phys. **14**, 7040 (2012).
[10] K. C. Smith and T. S. Fisher, Int. J. Hydrogen Energy **37**, 13417 (2012).
[11] Y. Jiao and S. Torquato, Phys. Rev. E **84**, 041309 (2011).
[12] M. Neudecker, S. Ulrich, S. Herminghaus, and M. Schröter, Phys. Rev. Lett. **111**, 028001 (2013).
[13] A. Jaoshvili, A. Esakia, M. Porrati, and P. M. Chaikin, Phys. Rev. Lett. **104**, 185501 (2010).
[14] S. Li, P. Lu, W. Jin, and L. Meng, Soft Matter **9**, 9298 (2013).
[15] S. Dagois-Bohy, B. P. Tighe, J. Simon, S. Henkes, and M. van Hecke, Phys. Rev. Lett. **109**, 095703 (2012).
[16] D. Bi, J. Zhang, B. Chakraborty, and R. P. Behringer, Nature (London) **480**, 355 (2011).
[17] G.-J. Gao, J. Bławzdziewicz, and C. S. O'Hern, Phys. Rev. E **74**, 061304 (2006).
[18] N. Xu and E. S. C. Ching, Soft Matter **6**, 2944 (2010).
[19] C. F. Schreck and C. S. O'Hern, in *Experimental and Computational Techniques in Soft Condensed Matter Physics*, edited by J. Olafsen (Cambridge University Press, Cambridge, 2010).
[20] A. W. Lees and S. F. Edwards, J. Phys. C **5**, 1921 (1972).
[21] M. Parrinello and A. Rahman, J. Appl. Phys. **52**, 7182 (1981).
[22] I. Souza and J. L. Martins, Phys. Rev. B **55**, 8733 (1997).
[23] S. Torquato and Y. Jiao, Phys. Rev. E **80**, 041104 (2009).
[24] H. C. Andersen, J. Chem. Phys. **72**, 2384 (1980).
[25] A. J. Liu and S. R. Nagel, Nature (London) **396**, 21 (1998).
[26] J. P. Bardet and I. Vardoulakis, Int. J. Solids Struct. **38**, 353 (2001).
[27] D. C. Liu and J. Nocedal, Math. Prog. B **45**, 503 (1989).
[28] P. Carbonetto, LBfgs—a MATLAB class for L-BFGS optimization, http://www.cs.ubc.ca/~pcarbo
[29] A. Haji-Akbari, M. Engel, A. S. Keys, X. Zheng, R. G. Petschek, P. Palffy-Muhoray, and S. C. Glotzer, Nature (London) **462**, 773 (2009).
[30] T. M. Truskett, S. Torquato, and P. G. Debenedetti, Phys. Rev. E **62**, 993 (2000).
[31] G. W. Delaney and P. W. Cleary, Europhys. Lett. **89**, 34002 (2010).
[32] Y. Jiao, F. H. Stillinger, and S. Torquato, Phys. Rev. E **81**, 041304 (2010).
[33] B. S. John, A. Stroock, and F. A. Escobedo, J. Chem. Phys. **120**, 9383 (2004).
[34] U. Agarwal and F. A. Escobedo, Nat. Mater. **10**, 230 (2011).
[35] F. Smallenburg, L. Filion, M. Marechal, and M. Dijkstra, Proc. Natl. Acad. Sci. USA **109**, 17886 (2012).
[36] M. S. Watanabe, Phys. Rev. E **51**, 3945 (1995).
[37] I. Srivastava, S. Sadasivam, K. C. Smith, and T. S. Fisher, J. Heat Transfer **135**, 061603 (2013).
[38] S. Torquato and Y. Jiao, Nature (London) **460**, 876 (2009).
[39] J. Baker and A. Kudrolli, Phys. Rev. E **82**, 061304 (2010).
[40] U. Agarwal and F. A. Escobedo, J. Chem. Phys. **137**, 024905 (2012).
[41] N. Volkov, A. Lyubartsev, and L. Bergstrom, Nanoscale **4**, 4765 (2012).
[42] Y. Cao, Probability Density Function (PDF) Estimator (V3.2), http://www.mathworks.com/matlabcentral/fileexchange/19121.